



Innovative carbon-free low content Pt catalyst supported on Mo-doped titanium suboxide (Ti_3O_5 -Mo) for stable and durable oxygen reduction reaction

Reza Alipour Moghadam Esfahani*, Svetoslava K. Vankova,
Alessandro H.A. Monteverde Videla, Stefania Specchia*

Politecnico di Torino, Department of Applied Science and Technology, Corso Duca degli Abruzzi, 24, 10129, Torino, Italy



ARTICLE INFO

Article history:

Received 2 May 2016

Received in revised form 21 July 2016

Accepted 16 August 2016

Available online 17 August 2016

Keywords:

Platinum

Titanium suboxides

Molybdenum

Oxygen reduction reaction (ORR)

Stability

ABSTRACT

Recently the use of titanium oxide and titanium suboxides (Magnéli phases) has been extensively investigated as an alternative catalyst support to carbon-based materials for the oxygen reduction reaction in low-temperature fuel cells. In this study, a 15 wt.% Pt-based catalyst was developed on a unique, stable mix of titanium suboxides, with a prevailing of the Ti_3O_5 phase, doped with Mo, as a Ti_3O_5 -Mo carbon-free support and compared to a commercial 20 wt.% Pt/C (E-TEK). The Pt/ Ti_3O_5 -Mo catalyst exhibits excellent electroactivity and stability toward the ORR, reaching a performance of 73.3 mA mg^{-1} , slightly more than the double of the commercial Pt/C, with a current density of 1.1 mA cm^{-2} at 0.9 V vs RHE , and an half-wave potential of 0.86 V vs RHE . A deep accelerated potential cycling between 0 and 1.2 V vs RHE up to 5000 cycles demonstrated the remarkable stability of the Pt/ Ti_3O_5 -Mo catalyst, whose electrochemical surface area loss was accounted for only 11%, compared to the more than 81% loss of the commercial Pt/C reference

© 2016 Elsevier B.V. All rights reserved.

1. Introduction

Platinum (Pt), which is a highly efficient catalyst, is widely applied in proton exchange membrane fuel cells (PEMFCs) as cathodic side for the oxygen reduction reaction (ORR: $O_2 + 4H^+ + 4e^- \rightarrow 2H_2O$). In the application of Pt catalysts, the supporting material is one of the most important factors when looking to enhance the electroactivity and stability of the catalyst. Carbon materials are extensively employed to support Pt catalysts in PEMFCs due to their excellent conductivity and high specific surface area. However, one of the main drawbacks of carbon supported catalysts is located at the cathode, which the electrode potential is relatively high in an acidic environment and carbon materials suffer corrosion under these conditions ($C + 2H_2O \rightarrow CO_2 + 4H^+ + 4e^-$, 0.207 V vs NHE at 25°C). As a consequence, dissolution and agglomeration of Pt particles occur resulting in a decrease of electroactivity of the catalyst [1–4]. The Pt dissolution, which is an anodic reaction, causes a mixed potential at the cathode and subsequently the negative shifting of the ORR reversible potential. As a result, a

huge decrease of the long-term stability of the catalyst performance occurs [1].

Among the candidates available for metal oxides supports, considerable attention has been paid to titanium suboxides (Ti_xO_{2x-1} , even known as Magnéli phases of titanium oxide) as a non-carbon material with high electronic conductivity, stability, and durability in acidic media. Substoichiometric Magnéli phases obtained from thermally treated TiO_2 in a reducing environment have electron conductivity similar to graphite thanks to oxygen vacancies in the crystalline lattice [5]. Moreover, chemically inert titanium suboxides materials are chosen because of economic reasons. These qualities make titanium suboxides an appropriate support for Pt-based catalyst utilization in PEMFC and DMFC [6–9], in particular for hydrogen fuel cell vehicles [5]. According to Walsh and Wills [10], the electrical conductivity of Ti_xO_{2x-1} depends on the suboxide 'x' value, but it is of the same order of magnitude as carbon. The electrical conductivity is greatest for $x = 3$ to 5, and it decreases at higher 'x' values. According to the literature, employing titanium suboxides instead of carbon as a support has the undoubted advantages of reducing the OH adsorption on Pt surface by lateral repulsion from the OH or O on the suboxide's support surface, and enhanced splitting of the O–O bond which is caused by the presence of oxygen vacancy sites on titanium suboxides support and preventing the dissolution of Pt from the surface of the

* Corresponding authors.

E-mail addresses: reza.alipour@polito.it (R. Alipour Moghadam Esfahani), stefania.specchia@polito.it (S. Specchia).

support [11–16]. Moreover, the presence of Ti^{3+} defects and/or oxygen vacancies in titanium suboxides can act as a charge electron recombination centers, with a beneficial role in catalysis and photocatalysis, by reducing the electron-hole pair recombination rate [17,18], and favoring the $d-d$ transition. Typically, titanium oxides containing Ti^{3+} show black or dark blue color because of the $d-d$ transition on Ti^{3+} [19,20].

Among all possible titanium suboxides, trititanium pentoxide (Ti_3O_5) has been extensively investigated, and it exists in a variety of structural polymorphs, as a potential material for oxygen sensor and for photocatalytic properties [21–23]. Trititanium pentoxide is a metal-like compound with high conductive properties (conductivity higher than 600 S cm^{-1}) [10,24].

Since TiO_2 is a very stable compound, the formation of titanium suboxides in reducing environment requires long exposure at very high temperatures ($>1200^\circ\text{C}$). The presence of a metal, such as Mo, Co, Ni, Cu, [1,5,21] favors the evolution of TiO_2 into Magnéli phases at much lower temperatures. Moreover, according to the literature [25–27], $\text{Ti}_x\text{O}_{2x-1}\text{-M}$ (with M=Co, Ni, Cu, Mo, Ru, Ir) as support plays a co-catalytic function together with Pt nanoparticles toward ORR. These supports not only solve the above-mentioned carbon-corrosion issues but also enhance the catalytic activity for ORR, due to strong metal-support interaction between the metal oxide and the Pt catalyst.

$\text{Pt}/\text{Ti}_3\text{O}_5\text{-Mo}$ exhibits excellent properties as a catalyst due to the structural and electronic properties of $\text{Ti}_3\text{O}_5\text{-Mo}$ [27–29]. In particular, $\text{Ti}_3\text{O}_5\text{-Mo}$ has a high resistance to electrochemical corrosion which enhances the durability of the Pt catalyst. The positive effect due to the trititanium pentoxide is explained by considering the changes in Pt- d electronic properties and the geometric effect that produces the contraction of Pt-Pt bonding distance [30,31], leading to a favorable condition for electrochemical reactions. The activity enhancement of binary $\text{Pt}/\text{Ti}_3\text{O}_5\text{-Mo}$ catalysts is attributed to the electronic donation of $\text{Ti}_3\text{O}_5\text{-Mo}$ to Pt surface, which modifies the electronic structure of Pt surface atoms resulting in a weakened interaction between Pt and intermediates, freeing more active sites for O_2 adsorption [32]. This results in strong physical and chemical interaction with adsorbed gas species [33–35]. Finally, in our recent studies, we found out that the presence of Ti_3O_5 suboxide in a series of Pt/C-TiOx-C catalysts positively improves the performance toward the ORR, enhancing the stability under potential cycling [36].

In this study, a comparative evaluation of the structure, composition and electrochemical performance of the $\text{Pt}/\text{Ti}_3\text{O}_5\text{-Mo}$ catalysts is discussed. A Pt layer was homogeneously deposited over the surface of the $\text{Ti}_3\text{O}_5\text{-Mo}$ support. The resulting $\text{Pt}/\text{Ti}_3\text{O}_5\text{-Mo}$ catalyst with intrinsic electrocatalytic activity and excellent stability in acidic media was applied toward the ORR. These efforts indicate that both Pt morphology and support structure can significantly enhance the catalytic activity and stability. The $\text{Pt}/\text{Ti}_3\text{O}_5\text{-Mo}$ catalyst was characterized by X-ray diffraction (XRD), inductively coupled plasma atomic mass spectroscopy (ICP-MS), X-ray photoemission spectroscopy (XPS), transmission electron microscopy (TEM), field-emission scanning electron microscopy (FESEM), UV-vis measurements, and electrochemical long-term activity testing, including cyclic voltammetry (CV), linear sweep voltammetry (LSV), and accelerated potential cycling test (APCT).

2. Experimental part

2.1. Chemicals

Titanium (IV) oxide, anatase (TiO_2) 99.8 wt.%, chloroplatinic acid hexahydrate ($\text{H}_2\text{PtCl}_6\cdot6\text{H}_2\text{O}$) $\geq 37.50\%$ Pt basis, sodium borohydride (NaBH_4) 98 wt.%, potassium hydroxide (KOH)

85 wt.%, ammonium hydroxide (NH_4OH) 28.0% NH_3 basis, polyvinylpyrrolidone (PVP40: $(\text{C}_6\text{H}_9\text{NO})_n$ average molar weight 40,000), poly(ethylene glycol)-block-poly(propylene glycol)-block-poly(ethylene glycol) (Pluronic® 123, average molar weight 5800), sulfuric acid (H_2SO_4) 95–98 wt.%, perchloric acid (HClO_4) 70 wt.%, Nafion® perfluorinated resin solution 5 wt.%, acetone (CH_3COCH_3) 99.5 wt.%, 2-propanol ($\text{C}_3\text{H}_8\text{O}$) 99.5 wt.%, and ammonium molybdate ($\text{H}_{24}\text{Mo}_7\text{N}_6\text{O}_{24}\cdot4\text{H}_2\text{O}$) were purchased from Sigma-Aldrich. A commercial platinum catalyst 20 wt.% on carbon black Vulcan XC-72R purchased from E-TEK was used for comparison tests. Nitrogen and oxygen gases were supplied in cylinders by SIAD with 99.999% purity. All aqueous solutions were prepared using ultrapure water obtained from a Millipore Milli-Q system with resistivity $>18 \text{ m}\Omega\text{ cm}$.

2.2. Synthesis of titanium suboxide ($\text{Ti}_3\text{O}_5\text{-Mo}$)

The titanium suboxide Ti_3O_5 was prepared by doping commercial TiO_2 anatase with Mo ions. TiO_2 was dispersed in a solution of (70:30 vol.%) ultrapure water and ethanol respectively, followed by the addition of 2 wt.% Pluronic P123 surfactant. The obtained solution was stirred for 5 h at ambient temperature. Then 10 wt.% of Mo ($\text{H}_{24}\text{Mo}_7\text{N}_6\text{O}_{24}\cdot4\text{H}_2\text{O}$) was added to the solution. The pH of the solution was held constant at pH=9 by adding NH_4OH . The mixed solution was continuously stirred at room temperature for other 5 h, evaporated at 120°C , and finally dried at 80°C for 12 h. The obtained powder was annealed at 850°C (heating rate of $10^\circ\text{C min}^{-1}$) for 8 h under a reducing atmosphere ($\text{H}_2:\text{N}_2$ 10:90 vol.%).

2.3. Synthesis of $\text{Pt}/\text{Ti}_3\text{O}_5\text{-Mo}$

100 mg of $\text{Ti}_3\text{O}_5\text{-Mo}$ support was dispersed in a solution of ultrapure deionized water and ethanol (30:10 mL) followed by adding 1 wt.% PVP surfactant. The solution was brought to pH 9–10 by adding NH_4OH and left stirring for 1 h. Then, 39.82 mg of $\text{H}_2\text{PtCl}_6\cdot6\text{H}_2\text{O}$ was dissolved in 10 mL of ultrapure deionized water and slowly reduced by adding 1 wt.% NaBH_4 at room temperature. This was then added to the support solution and left stirring for 5 h at an ambient temperature. The obtained solution was sonicated for 1 h and later left to stir for 5 h to allow for Pt adsorption. The resulting catalyst obtained after drying was heat-treated at 450°C (heating rate of 5°C min^{-1}) for 5 h under a reducing atmosphere ($\text{H}_2:\text{N}_2$ 10:90 vol.%).

2.4. Chemical-physical characterization

The platinum-to-support weight percentage in the synthesized $\text{Pt}/\text{Ti}_3\text{O}_5\text{-Mo}$ catalyst was determined by ICP-MS with a ThermoFisher Scientific ICAP-Q instrument. Prior to analysis, the samples were digested in hot concentrated HCl/HNO_3 3:1 mixture with some droplets of H_2SO_4 .

The XRD patterns were recorded on a Panalytical X'Pert PRO diffractometer with a PIXcel detector, using $\text{Cu K}\alpha$ radiation ($\lambda = 0.15418 \text{ nm}$), under the operating conditions of $2\theta = 20^\circ - 90^\circ$ and 2θ step size = 0.03, in order to examine the different polymorphs. The markers were located using the Philips X'Pert HighScore Software (ICDD database). The morphology of the support and the catalysts, and the characterization of the metals were observed by FESEM (JEOL-JSM-6700F instrument coupled with an energy dispersive X-ray spectroscopy (EDX) detector by OXFORD INCA). For the support, the STEM modality was employed to better enlighten the presence of Mo. The support was deposited on a copper grid with a graphitic carbon layer. TEM was carried out using a JEOL-2000 FXII microscope equipped with a LaB6 gun. 0.5 mg of samples was dispersed in 5 mL isopropyl alcohol and sonicated for

3 h, later, 5 μ L of the solution was dropped on the surface of the copper grid and dried under N_2 atmosphere.

Diffuse Reflectance (DR) UV-vis spectra of outgassed commercial TiO_2 and synthesized Ti_3O_5 -Mo were performed (Agilent Cary 5000 UV-vis-NIR spectrometer) to measure the optical absorption and band gap values by applying the Tauc equation.

XPS analysis was performed to determine the elemental surface composition of the catalysts. The analysis was carried out using a Physical Electronics PHI 5000 Versa Probe electron spectrometer system with monochromated $Al K\alpha$ X-ray source (1486.60 eV) running at 15 kV and 1 mA anode current. The survey spectra were collected from 0 to 1200 eV. The narrow Pt 4f spectra were collected from 60 to 90 eV, the narrow Mo 3d spectra from 220 to 248 eV, and the narrow Ti 2p spectra from 444 to 480 eV. All of the spectra were calibrated against a value of the C 1 s binding energy of 284.5 eV. Multipack 9.0 software was used for obtaining semi-quantitative atomic percentage compositions, using Gauss-Lorentz equations with the Shirley-type background. A 70%/30% Gaussian/Lorentzian line shape was used to evaluate peaks position and areas of the high-resolution spectra.

2.5. Electrochemical characterization

The catalysts were characterized using CV, LSV, and CO stripping voltammetry measurements. All the electrochemical characterizations were carried out in a three-compartment electrochemical cell using a multi-potentiostat (Bio-Logic SP150), and a rotating disk electrode mounted on a rotating ring disk electrode apparatus (RRDE-3A ALS Model 2323). As the electrolyte, both a 0.5 M H_2SO_4 and a 0.1 M $HClO_4$ aqueous solutions were used and saturated with either N_2 or O_2 pure gas by direct bubbling into the solution. For RDE measurements, the cell was equipped with a glassy carbon (GC) disk working electrode (0.07 cm^2 geometric area), a carbon graphite as a counter electrode and a reference hydrogen electrode (RHE).

The catalyst ink was prepared dissolving 7.0 mg of the catalyst in 0.6 mL of H_2O , 1 mL of isopropyl alcohol IPA and using an ionomer-to-catalyst (ITC) mass ratio (mg of Nafion® over mg of catalyst) equal to 0.1 and calculated Pt quantity loading of $15 \mu\text{g}_{\text{Pt}} \text{ cm}^{-2}$, corresponding to 3 μL of the sonicated ink. This mixture was sonicated for 30 min and then stirred for 2 h. Then, the catalyst ink was pipetted onto a glassy carbon electrode so that the catalyst film contained 76.9 nmol of Pt. The working electrode was polished with 1 and 0.06 mm alumina powders to mirror-like finish its surface and sonicated to remove alumina particles before each experiment.

CV was recorded in N_2 -purged 0.5 M H_2SO_4 and 0.1 M $HClO_4$ to obtain the background capacitive current and the electrochemical surface area (ECSA) of the Pt catalyst which was conducted at room temperature and a scan rate of 10 mV s^{-1} . To clean the surface of Pt catalyst, each electrode was cycled 30 times in N_2 -purged 0.5 M H_2SO_4 , sweeping in the potential range of 0.0–1.5 V vs RHE at a scan rate of 100 mV s^{-1} . The ECSA ($\text{m}^2 \text{ g}^{-1}$) of the catalysts was determined from the Pt-hydrogen desorption region between 0.0 V and 0.4 V vs RHE, by integrating the total charge, normalizing with scan rate, Pt loading, and assuming a surface charge density of $210 \mu\text{C cm}^{-2}$ for a monolayer adsorption of hydrogen on Pt surface [4,43].

CO-stripping voltammetry was performed in 0.5 M H_2SO_4 and 0.1 M $HClO_4$ at a scan rate of 20 mV s^{-1} . Prior to the analysis, a flow rate of CO was pre-adsorbed for 15 min while the working electrode was maintained at the constant potential of 0.06 V vs RHE. Afterward, a flow rate of pure N_2 was introduced for 20 min to remove the CO dissolved in the solution before stripping the CO. LSV was conducted in 0.5 M H_2SO_4 and 0.1 M $HClO_4$ solution by bubbling O_2 gas at room temperature at a scan rate of 5 mV s^{-1} and rotating disk speed of 900 rpm. O_2 was bubbled directly into the cell

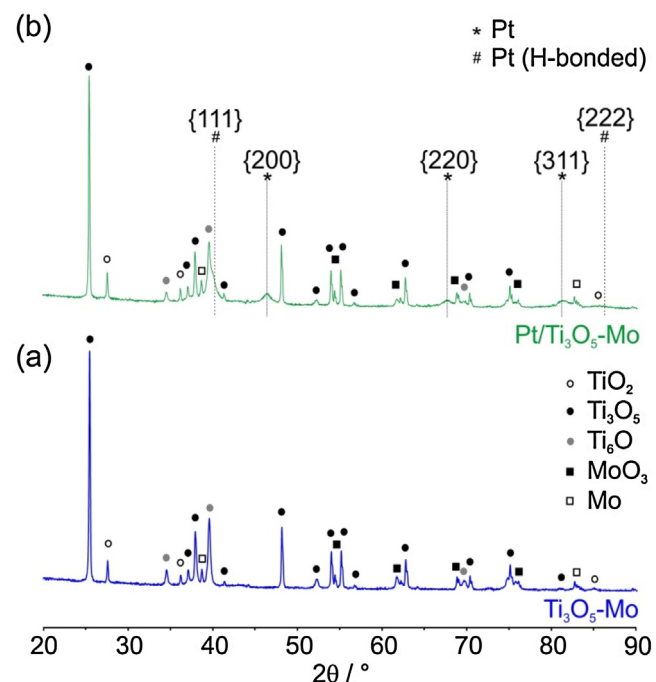


Fig. 1. XRD diffractograms of the Ti_3O_5 -Mo support (a), and of the Pt/Ti_3O_5 -Mo catalyst (b).

for at least 30 min before the test and was flushed over the cell solution during the measurement. An electrochemical impedance spectroscopy (EIS) measurement was taken at OCV, with a wave amplitude of 10 mV and frequencies in the range of 10 kHz–100 mHz, for the evaluation of the high-frequency resistance (R) of the materials developed.

The stability of the Pt/Ti_3O_5 -Mo catalyst and of the Ti_3O_5 -Mo support were addressed through APCT by performing 5000 cycles varying the potential in the range of 0–1.2 V vs RHE at a scan rate of 50 mV s^{-1} , in an N_2 -saturated 0.5 M H_2SO_4 solution [37–39]. According to the DOE protocols [40], this potential range assures the accelerated corrosion of the support as well as the sintering of Pt nanoparticles. For comparison purposes, the stability of the commercial Pt/C was tested in the same conditions, as well, up to 2500 potential cycles. UV-vis measurements were performed on aqueous electrolyte before and after APCT to verify the stability of the Ti_3O_5 -Mo, by assessing the absence of Mo and Ti into the solution.

3. Results and discussion

3.1. Physical-chemical characterization of the Ti_3O_5 -Mo support and the Pt/Ti_3O_5 -Mo catalyst

The crystallographic structure of the materials synthesized is shown in Fig. 1. Fig. 1(a) shows the peak orientation referring to Ti_3O_5 which was synthesized via Mo doping of anatase TiO_2 at high temperature. In fact, the reduction of TiO_2 to Ti_3O_5 is favored at high temperature, higher than 1200°C . [21]. The presence of Mo favors the formation of the suboxides in a reducing environment at much lower temperature, 850°C , as in our case. The corresponding diffractogram displays the Ti in a reduced form, mainly as trititanium pentoxide Ti_3O_5 phase (ICDD card no. 01-072-2101) with $Cmcm$ orthorhombic structure (main characteristic reflection at $2\theta = 25.5^\circ$, {110}). Titanium suboxide phase Ti_6O (ICDD card no. 01-072-1471) is also present, together with few TiO_2 rutile phase (ICDD card no. 01-088-1173). Thus, our support is a mix of Ti_3O_5 , Ti_6O , and TiO_2 , with Ti_3O_5 being the prevailing Ti sub-

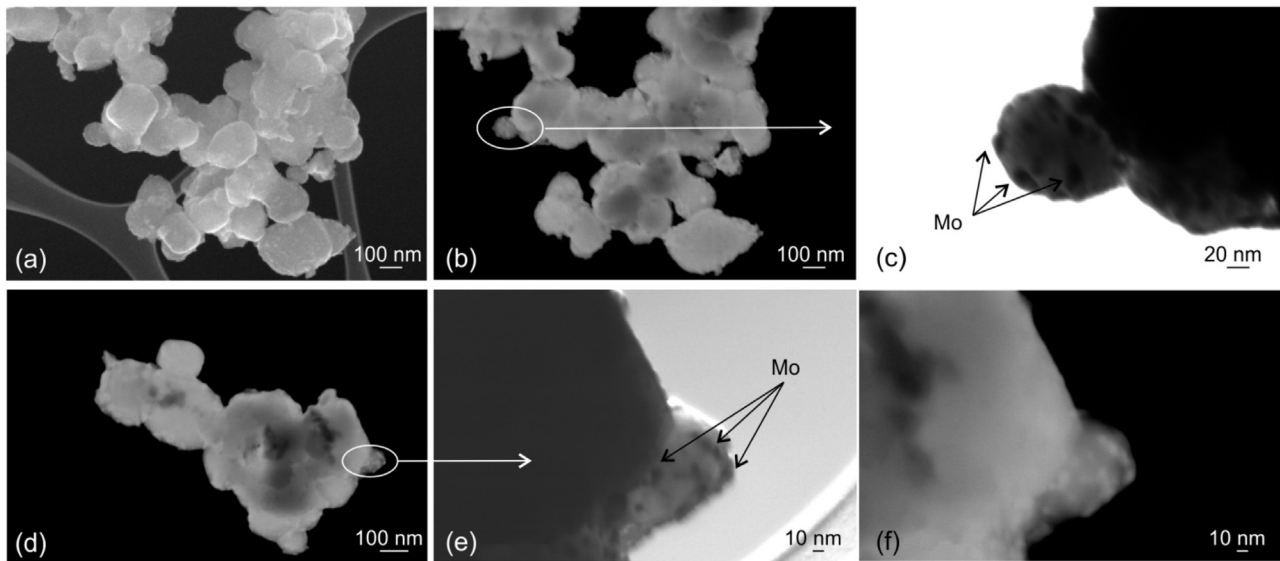


Fig. 2. FESEM-STEM images of two different areas (a/b/c and d/e/f) of the Ti_3O_5 -Mo support, at different magnifications to enlighten Mo nanoparticles.

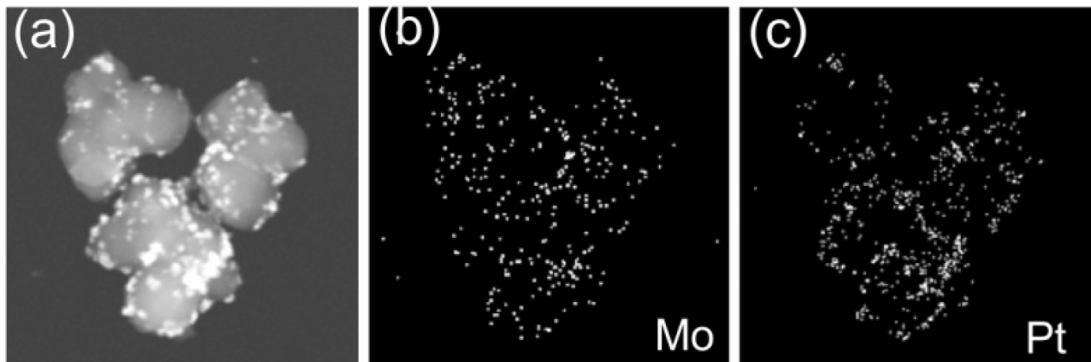


Fig. 3. Back-scattered FESEM image of the $\text{Pt}/\text{Ti}_3\text{O}_5$ -Mo catalyst (a) with EDX measurements of the Mo (b) and Pt (c) distribution.

oxide phase. Mo is present either as metallic Mo (ICDD card no. 01-088-2331) and MoO_3 (ICDD card 00-021-0569). According to the literature, Ti_3O_5 is a polymorphic compound that can crystallize in several crystallographic phases (α , β , γ , δ) [41]. The orthorhombic structure of the trititanium pentoxide was expected, since, after exposition at a temperature higher than 250°C , the Ti_3O_5 turns into the orthorhombic phase (space group Cmcm), and based on semiconductor–metal transition theory, the compound should exhibit metallic behavior [19,22,23,41,42].

Fig. 1(b) shows the peaks of the $\text{Pt}/\text{Ti}_3\text{O}_5$ -Mo catalyst, with the corresponding reflections of metallic platinum with face-centered cubic structure. Reflections of Pt are present as pure Pt (ICDD card no. 01-087-0640), with typical reflections at $2\theta = 46.5^\circ$ {200}, 67.9° {220}, and 81.6° {311}, and as Pt H-bonded (ICDD card no. 01-087-0636), with typical reflections at $2\theta = 40.0^\circ$ {200} and 85.8° {222}. The Pt-H bonded, or [H]-loaded Pt [43] is the synonym for hydrogenated Pt [44,45]. In fact, heating the catalyst at temperatures higher than 50°C in a reducing atmosphere (in our case: 450°C in $\text{H}_2:\text{N}_2$) implies the hydrogenation Pt. Under low saturation a H_2 coordination leads to H–H bond breaking and formation of H–Pt–H hydrides, which agrees with one of the possible reaction pathways of H_2 side-on cleavage on Pt [46,47]. However upon high saturation, H_2 molecules symmetrically bind to Pt clusters and remain dimerized [48].

The Pt crystallites size over Ti_3O_5 -Mo was calculated as average value from the width of the {200}, {220}, and {311} peaks using

the Scherrer-Debye equation [49,50], resulting in a mean crystallite size of Pt equal to 14 nm. The same calculation on the {111} and {222} peaks of the H-loaded Pt provided a mean crystallite size of Pt equal to 5 nm. The two average values obtained are in fairly good agreement with TEM analysis shown in Fig. 2(d)–(f).

Fig. 2 shows FESEM-STEM images of the Ti_3O_5 -Mo support in different areas. The STEM modality allows appreciating the fine distribution of Mo in very small metallic particles. Mo particles cover the entire surface of the support, in a homogeneous way. Fig. 3 shows FESEM-EDX images of the $\text{Pt}/\text{Ti}_3\text{O}_5$ -Mo, confirming the homogeneous distribution of Pt and Mo nanoparticles over the surface of the support. Fig. 4 shows TEM images at different magnifications of Ti_3O_5 -Mo (a, b, and c) and $\text{Pt}/\text{Ti}_3\text{O}_5$ -Mo (d, e, and f). The Ti_3O_5 -Mo support has a well-dispersed series of Mo nanoparticles on the surface of the Ti_3O_5 . Mo nanoparticles are in the range of 10–15 nm, confirming the results from FESEM-STEM analysis. Also the $\text{Pt}/\text{Ti}_3\text{O}_5$ -Mo catalyst has good dispersion and small particle size of Pt, in agreement with XRD and FESEM-EDX analysis.

The XPS high-resolution spectra of the $\text{Pt}/\text{Ti}_3\text{O}_5$ -Mo catalyst confirm the presence of Ti_3O_5 on the surface of the support (Fig. 5). The center of Ti^{3+} peak, shown in Fig. 5(a) was located at a binding energy of 457.3 eV, attesting to the presence of Ti_3O_5 . The centers of the Ti^{4+} with 2 $p_{3/2}$ and 2 $p_{1/2}$ doublet peaks correspond to the binding energies of 459.1 and 464.7 eV, respectively, characteristic of the presence of TiO_2 phase [51–53]. The Mo high-resolution spectrum in Fig. 5(b) shows the Mo^{6+} as the dominant state with

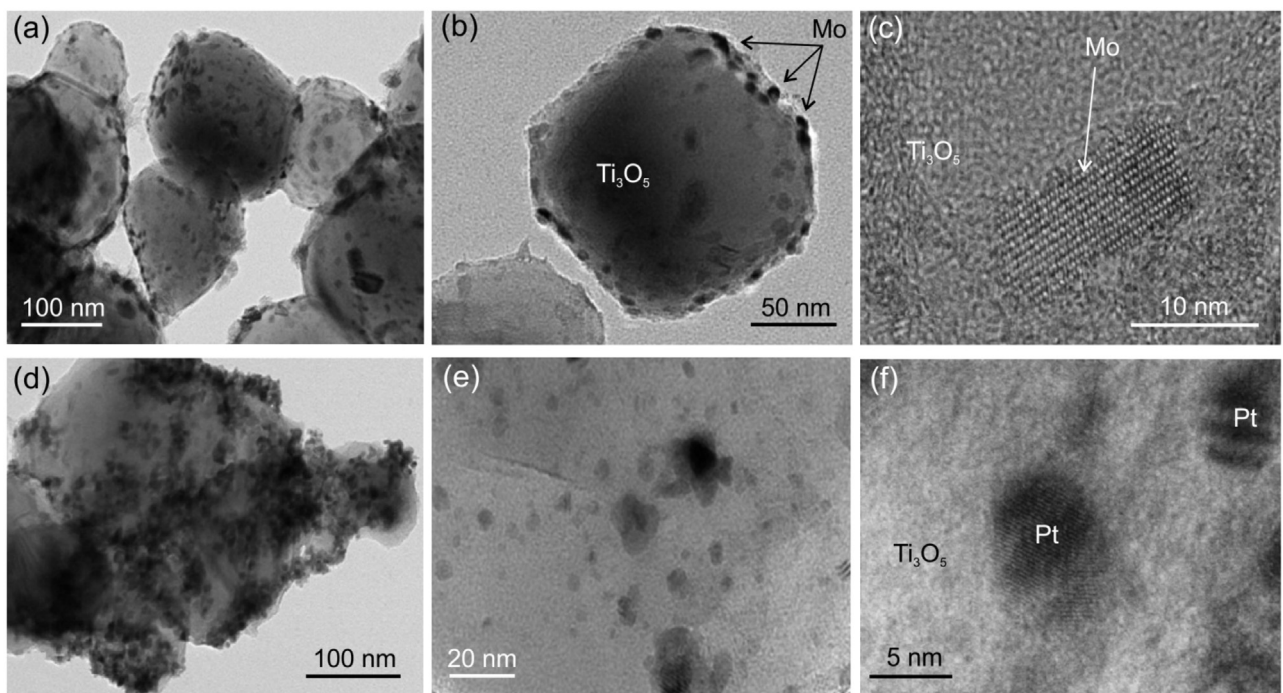


Fig. 4. TEM images of the Ti₃O₅-Mo support (a, b, and c) and of the Pt/Ti₃O₅-Mo catalyst (d, e, and f).

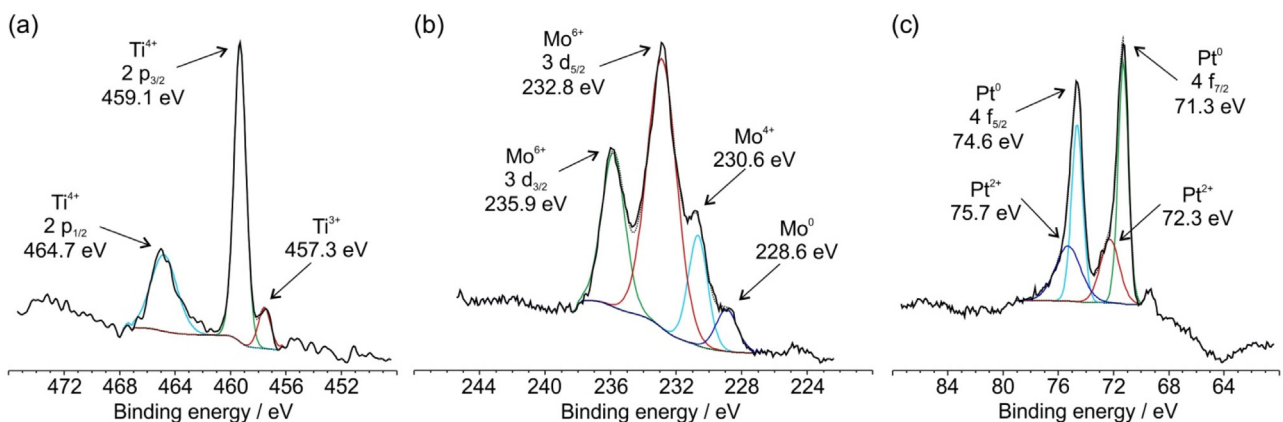


Fig. 5. XPS high-resolution spectra of the Pt/Ti₃O₅-Mo catalyst: Ti (a), Mo (b), and Pt (c).

3 d_{5/2} and 3 d_{3/2} doublet peaks at binding energies of 232.8 eV and 235.9 eV respectively: the peak difference of 3.1 eV is due to the spin-orbit coupling. The Mo metallic and Mo⁴⁺ have lower relative intensity at 228.6 eV and 230.6 eV, respectively [54,55]. The Pt high-resolution spectrum shown in Fig. 5(c) demonstrates spin-orbit splitting doublet peaks in the 4 f region referring to 4 f_{7/2} and 4 f_{5/2}, where the deconvolution of the Pt spectrum reveals two pairs of doublet peaks at each region. The high intense doublet peaks at the binding energies of 71.3 eV and 74.6 eV, respectively, are attributed to metallic Pt. The low-intensity doublet peaks at binding energies of 72.3 eV and 75.7 eV, respectively, appear at 1.2 eV higher in binding energy than that of Pt⁰, assigned to Pt²⁺ species due to surface oxide/hydroxide [55,56]. Besides, the curve fitting of Pt 4 f_{7/2} reveals 0.3 eV positive shift towards higher binding energy compared to the 4 f_{7/2} value of pure Pt, which can be attributed to the positive charge on the dispersed Pt particles interacting with the oxide support [55,57].

The loading of the Pt over the Ti₃O₅-Mo was equal to 15 wt.%, verified by ICP-MS analysis.

Finally, the optical band gap of the starting TiO₂ and the Ti₃O₅-Mo support was estimated based on the absorption spectra of the diffuse reflectance of the two materials. The reflectance data were converted into the absorption coefficient values according to the Kubelka-Munk equation, as shown in Fig. 6(a) [58,59]. The Ti₃O₅-Mo support has better light spectra absorbance than the starting TiO₂. The band gap of the two materials was estimated by applying the Tauc relation, plotting the transformed Kubelka-Munk function as a function of the energy of the excitation source for an indirect semiconductor, Fig. 6(b) [60–63]. The band gap of the Ti₃O₅-Mo support, 2.6 eV, is lower compared to that of TiO₂, 3.2 eV. The reference literature value for bulk anatase TiO₂ is 3.23 eV at 384 nm [61,64], indicating the better conductive properties of the support. Of course, this value is still far from the band gap value of pure Ti₃O₅ in the orthorhombic state, ranging from 0.07 to 0.15 eV [19,23,65] with a behavior equivalent to a metal conductor. In fact, in this case according to XRD and XPS analyses, the Ti₃O₅-Mo support contains a mixture of Ti₃O₅, Ti₆O, and TiO₂, with the presence of the Ti³⁺ defects and/or oxygen vacancies. In fact, according to the literature

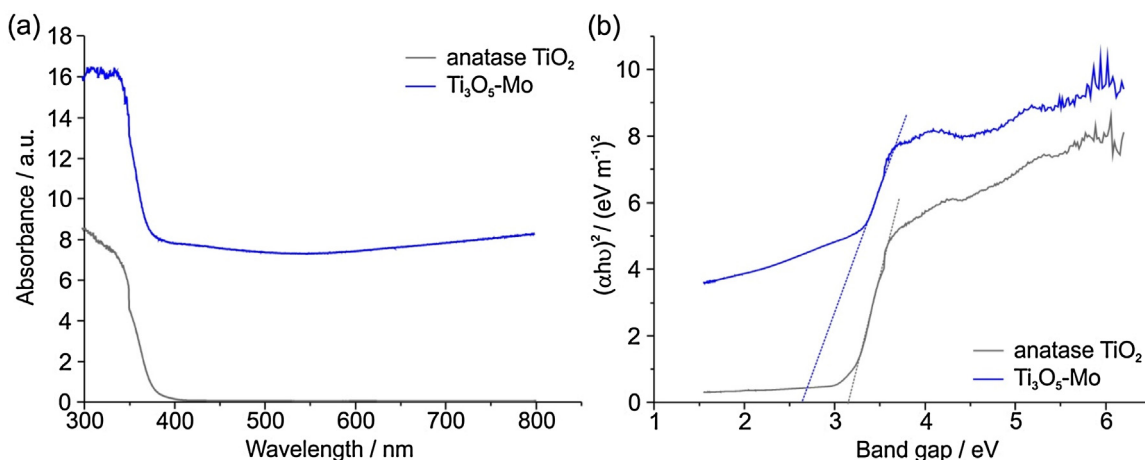


Fig. 6. (a) Diffuse reflectance UV-vis spectra according to the Kubelka–Munk equation and (b) transformed Kubelka–Munk function vs. energy of the excitation source (Tauc plot for the indirect allowed transition) of the starting anatase TiO₂ and Ti₃O₅-Mo support.

[17–20], Ti³⁺ defects and oxygen vacancies are responsible for the *d*-*d* transition. The presence of Ti³⁺ species is essential to provide proper electronic conductivity [66]. Definitely, the dark gray color of the Ti₃O₅-Mo support, and the black color of the Pt/Ti₃O₅-Mo catalyst is an indirect confirmation of the presence of Ti³⁺ as well [19]. Last but not least, the molybdenum has a synergistic effect, enhancing the catalytic and photocatalytic properties of the starting materials [25,67]. In fact, doping with some transition metals such as Mo⁶⁺, W⁶⁺, and Fe³⁺ plays a favorable effect and the energy gap of TiO₂ can be efficiently narrowed [68,69].

3.2. Electrochemical characterization of the Pt/Ti₃O₅-Mo catalyst

Fig. 7 shows the CVs for Pt/Ti₃O₅-Mo and commercial Pt/C catalysts in 0.5 M H₂SO₄ and 0.1 M HClO₄ measured at 25 °C. The Pt/Ti₃O₅-Mo catalyst shows well-known hydrogen ad/desorption characteristics in both electrolytes. Three anodic peaks and three cathodic peaks with reversibility in hydrogen region were assigned to polycrystalline Pt particles over the surface of the support. For both catalysts the polarisation curves exhibit three characteristic regions: the hydrogen ad/desorption peak at low potential range, the double layer capacitance region, and the Pt oxide formation region at high potential, due to the adsorption of oxide/hydroxide on Pt surface. On the other hand, a well-defined cathodic peak at 0.83 and 0.72 V for Pt/Ti₃O₅-Mo and Pt/C in sulfuric acid, and 0.86 and 0.80 V for Pt/Ti₃O₅-Mo and Pt/C in perchloric acid, respectively, can be attributed to desorption of oxide/hydroxide layer from the Pt surface. The values of the charge transfer resistance of the supports employed, measured via EIS at OCV in the presence of sulfuric acid as electrolyte, were accounted as 6.2 Ω for the Ti₃O₅-Mo (5.8 Ω without Nafion® in the ink), 7.5 Ω for the TiO₂-anatase, and 7.9 Ω for the carbon black (E-TEK). The ESCA of the catalysts, which is determined by the magnitude of the corresponding charge from the hydrogen electro-oxidation peaks (by applying a conversion factor of 210 μC cm⁻²) after subtraction of the double layer capacitance, are listed in Table 1, showing a higher value for the Pt/C in sulfuric acid compared to Pt/Ti₃O₅-Mo catalyst. Interestingly, the ECSA values in perchloric acid are higher than that in sulfuric acid. The higher ECSA values in perchloric acid are mainly due to the non-adsorbing or weakly adsorbing properties of HClO₄ as electrolyte [70–73]. The lower ECSA value of Pt/Ti₃O₅-Mo compared to Pt/C can be attributed to the low specific surface area of the Pt/Ti₃O₅-Mo, around 10 m² g⁻¹, because of the prolonged heat treatment under H₂/N₂ atmosphere to form oxygen vacancies. Similar values were

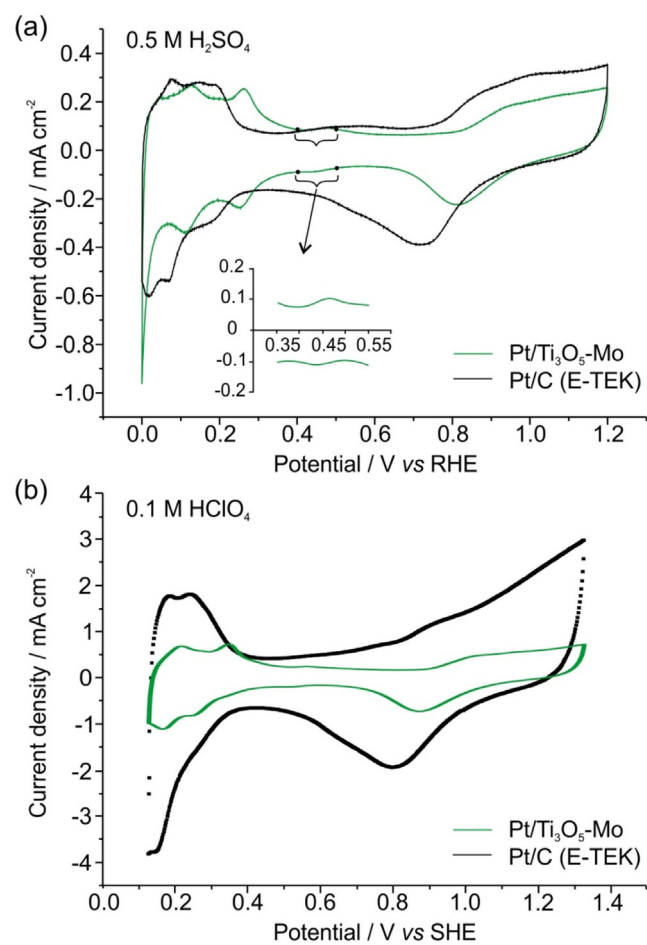


Fig. 7. CV of the Pt/Ti₃O₅-Mo and Pt/C recorded in 0.5 M H₂SO₄ (a), and in 0.1 M HClO₄ (b). For both cases: scan rate of 10 mV s⁻¹ at 25 °C (catalyst loading: 15 μg_{Pt} cm⁻², 0.1 ITC mass ratio).

obtained for Pt/TiO_x-C catalysts heat treated at 1000 °C in reducing atmosphere [36].

Moreover, the CV of Pt/Ti₃O₅-Mo in sulfuric acid shows redox peaks between 0.38 and 0.52 V vs RHE. These peaks are attributed to the faradaic process of intercalation/de-intercalation of H atoms into MoO_y lattice, with formation hydrogen molybdenum bronzes. This is due to the well-known fact which MoO_y in the presence of

Table 1

Electrochemical characterization of Pt/Ti₃O₅-Mo and Pt/C (E-TEK) catalysts in 0.5 M H₂SO₄ and 0.1 M HClO₄ as electrolytes. Data calculated from Figs. 7–9.

	Pt [mg cm ⁻²]	Q _H [mC cm ⁻²]	ECSA _{H2} @ H ₂ SO ₄ [m ² g ⁻¹]	ECSA _{H2} @ HClO ₄ [m ² g ⁻¹]	ECSA _{CO} @ H ₂ SO ₄ [m ² g ⁻¹]	I @ 0.9 V, H ₂ SO ₄ [mA cm ⁻²]	Specific activity @ 0.9 V, H ₂ SO ₄ [mA cm _{Pt} ⁻²]
Pt/Ti ₃ O ₅ -Mo	0.015	0.540	22.3	33.1	66.3	1.1	2.1
Pt/C (E-TEK)	0.020	0.616	39.5	44.2	70.4	0.7	0.3

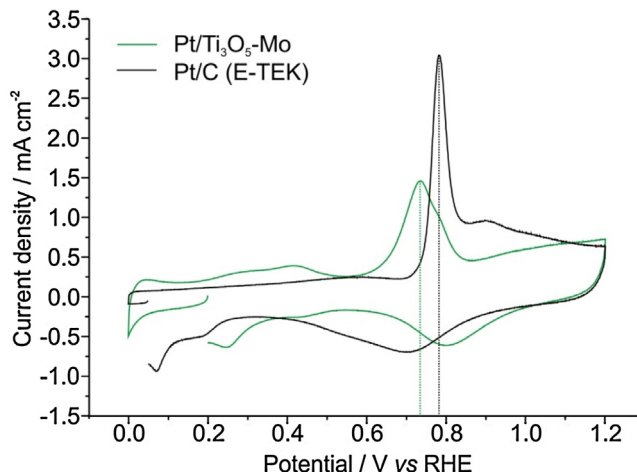


Fig. 8. CV of CO oxidation on Pt/Ti₃O₅-Mo and Pt/C E-TEK recorded in 0.5 M H₂SO₄, scan rate of 20 mV s⁻¹ at 25 °C (catalyst loading: 15 µg_{Pt} cm⁻², 0.1 ITC mass ratio).

noble metals absorbs the hydrogen at room temperature and forms H_xMoO_y: xH⁺ + xe⁻ + MoO_y ↔ H_xMoO_y [55,74–76].

The hydrogen evolution reaction (HER) of Pt/Ti₃O₅-Mo in sulfuric acid (Fig. 7a) occurs at slightly lower potential range compared to Pt/C. The reasons could lie in the electrical conductivity of the Ti₃O₅-Mo support. In fact, according to the band gap measurements (Fig. 6), Ti₃O₅-Mo has a higher band gap valued compared to the theoretical value of the Ti₃O₅, sign that the support is accompanied by other compounds which affect the electrical conductivity. Indeed, XRD analyses showed that the support is a mix of Ti₃O₅, Ti₆O, and TiO₂, with Ti₃O₅ being the prevailing Ti suboxide phase. This fact could explain the shift of the HER. Moreover, the presence of Mo, both in the form of metallic Mo and MoO₃, could play a role in the shift of the HER, as explained in the literature [6,8,37,77,78]. Furthermore, according to Markovic et al. [79] the under-potentially deposited hydrogen, H_{upd}, and the weakly adsorbed states as the reactive intermediate, H_{ad}, could play a role as well. In fact, the H_{upd} is strongly dependent on the crystallographic orientation of the Pt surface [80]. The weakly adsorbed state of H_{ad} on Pt single crystals could couple to the strongly adsorbed state of the H_{upd}, with a consequent indirect effect of the H_{upd} on the kinetics. Thus, H_{upd} might play an important role in the kinetics of the HER, and the HOR as well, in aqueous electrolyte solutions.

To investigate the influence of the suboxide support on Pt catalyst in the presence of CO species, a CO stripping test was performed for both catalysts, Pt/Ti₃O₅-Mo and Pt/C, in 0.5 M H₂SO₄ at 25 °C, as shown in Fig. 8. The results of CO stripping over Pt/Ti₃O₅-Mo catalyst show the onset potential corresponding to the CO oxidation reaction shift toward the lower potential value, with the peak potential appearing at 0.74 V vs RHE while for Pt/C the peak potential appeared at 0.79 V vs RHE. Apart from the main oxidation peak, there is a minor pre-peak at a lower potential for Pt/Ti₃O₅-Mo, as an early onset potential, due to the oxidation of weakly bonded CO. The early onset of CO oxidation as a pre-peak is typical of catalysts alternating Pt-containing layers and layers containing suboxides of a second metal, such as Ti, Ta, W, and Mo [81,82]. The results indicated the Ti₃O₅-Mo support, through the oxygen vacancies which

formed in close contact to Pt nanoparticles, could supply a source of hydroxyl intermediates (OH) which extends the active surfaces for oxidation of CO to CO₂ and polishing the Pt active site from CO poisoning species [16,83,84]. Moreover, since the CO species can only be adsorbed on the surface of the Pt atoms (active site), the CO oxidation charge can be converted into the surface area by applying a conversion factor of 420 µC cm⁻², as used for polycrystalline Pt [85,86]. Consequently, the active Pt surface area of the electrodes are 1.25 cm_{Pt}² and 1.77 cm_{Pt}² for Pt/Ti₃O₅-Mo and commercial Pt/C, respectively. These values, converted into m² g⁻¹, are listed in Table 1 for a comparison with the ECSA values calculated from the hydrogen underpotential deposition.

The ORR is a complex multi-step reaction involving the exchange of four electrons to form water, which is the desired reaction pathway [87]. Fig. 9(a) and (b) shows the ORR activities of Pt/Ti₃O₅-Mo and Pt/C catalysts in 0.5 M H₂SO₄ and 0.1 M HClO₄, respectively, at 25 °C purged by O₂ at 900 rpm. The activity of the sole support, Ti₃O₅-Mo, is reported as well for comparison purposes. In sulfuric acid the Pt/Ti₃O₅-Mo catalyst exhibits considerable activity toward ORR with a high onset potential of O₂ reduction as well as a half-wave potential, which is achieved at 0.86 V vs RHE (compared to a half-wave potential of 0.84 V vs RHE for the commercial Pt/C). The ORR polarisation curve shows that both catalysts display diffusion control when the potential is less than 0.65 V vs RHE, reaching limiting current densities between 3–3.5 mA cm⁻². The lower values of the limiting currents at 900 rpm in sulfuric acid for both catalysts could be linked with the adsorbing properties of H₂SO₄ as electrolyte. In fact, the sulfate, and phosphate, anion adsorption poisons the Pt surface. As a consequence, it is expected that the activity in sulfuric acid decreases dramatically. Interestingly, according to the literature, Pt/Ti-suboxides catalysts are able to counteract the anion adsorption poisoning due to surface modification of Ti-suboxides by sulfate anions, which increase the charge transfer of the support by modifying the electric conductivity [15,52,88–90].

In perchloric acid the Pt/Ti₃O₅-Mo catalyst exhibits slightly lower activity toward ORR compared to Pt/C, with a half-wave potential of 0.85 V vs SHE (compared to a half-wave potential of 0.90 V vs SHE for Pt/C). The ORR polarisation curves show that both catalysts display the diffusion control region for potential lower than 0.65 V vs RHE, reaching the expected limiting current densities around 4.3 mA cm⁻² at 900 rpm.

The specific activity of the Pt/Ti₃O₅-Mo, and Pt/C in sulfuric acid was calculated determining the ORR kinetic current i_k considering the mass transport, using the relationship established by the Koutecky–Levich theory, and normalizing with the specific surface area of Pt. The activity of electrocatalysts was calculated from the experimental data using the mass-transport correction for rotating disk electrodes. The calculated values at 0.9 V vs RHE, listed in Table 1, are 2.1 mA cm_{Pt}⁻² for Pt/Ti₃O₅-Mo and 0.3 mA cm_{Pt}⁻² for Pt/C, respectively.

For ORR mechanism understanding, the LSV were collected at different rotational speeds, both in sulfuric and perchloric acid, as shown in Fig. 9(c) and (d), respectively. Diffusion-limited current densities collected at different rotation rates in the potential range from 0.2 to 0.8 V vs RHE were used to determine the number of electrons transferred associated with ORR, which was calculated

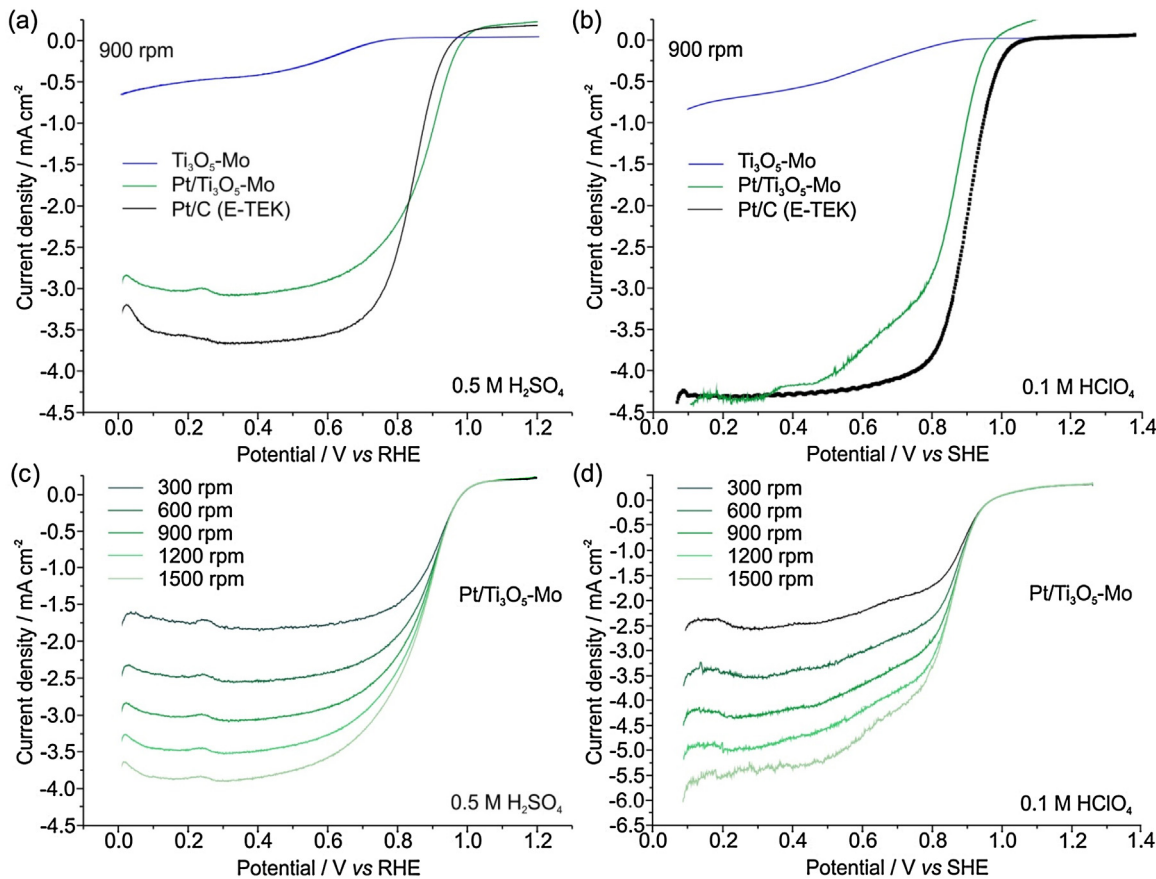


Fig. 9. ORR for Ti₃O₅-Mo, Pt/Ti₃O₅-Mo, and Pt/C (E-TEK) recorded at a scan rate of 5 mV s⁻¹ at 25 °C and 900 rpm (Pt loading: 15 µg_{Pt} cm⁻², 0.1 ITC mass ratio) in 0.5 M H₂SO₄ (a) and 0.1 M HClO₄ (b). ORR for Pt/Ti₃O₅-Mo at different rotational speeds in 0.5 M H₂SO₄ (c) and 0.1 M HClO₄ (d).

to be almost 4 (from 3.86 to 4.17) by the Koutecky–Levich equation in sulfuric acid (not shown here), suggesting a complete reaction to water with a very limited hydrogen peroxide production.

Overall, the Pt/Ti₃O₅-Mo showed promising performance with a mass activity of ~73 mA mg_{Pt}⁻¹, which is almost double of the Pt/C benchmark catalyst, in agreement with literature data [5,85].

3.3. Stability of the Pt/Ti₃O₅-Mo catalyst

Besides high electrocatalytic activity, the stability of the catalyst is an important characteristic that was evaluated for the Ti₃O₅-Mo support, the Pt/Ti₃O₅-Mo catalyst, and the commercial Pt/C, as well (Fig. 10). The stability of the Ti₃O₅-Mo and Pt/Ti₃O₅-Mo was assessed up to 5000 potential cycling in sulfuric acid. The Ti₃O₅-Mo is perfectly stable in 0.5 M H₂SO₄ aqueous electrolyte over the full range of applied potential cycling, Fig. 10(a). The CV curves have nearly rectangular shapes with small reversible redox peaks, typical for pseudo-capacitive materials [29]. The Pt/Ti₃O₅-Mo, Fig. 10(b), shows limited loss of performance. The double layer region shows constant capacity for all cycles, a sign that the Ti₃O₅-Mo support is a stable and durable support. Instead, Fig. 10(c), the Pt/C shows a huge performance decay just after 2500 cycles, with a noticeable reduction of the hydrogen desorption-adsorption peaks, demonstrating the commercial catalyst as an unstable catalyst for ORR.

Fig. 11 shows the losses of ECSA calculated from Fig. 10, for the two Pt-based catalysts. The Pt/Ti₃O₅-Mo the ECSA loss was very limited after 5000 APCT cycles, only 11.2%. In fact, according to the literature [13,36,37,91–93], the Ti₃O₅ suboxide available on the surface of the catalyst does not contribute during hydrogen ad/desorption regime but has a major influence on the stability of

the catalyst itself. No Ti oxidation was observed during the CVs performance, Fig. 10(a), a sign that Ti₃O₅-Mo remained stable. For the Pt/C, as expected, notwithstanding the higher starting ECSA value, it reduced dramatically because of the corrosion of the carbon support and the consequent Pt particles migration and sintering, reaching an overall ECSA loss of more than 81%.

To further assess the stability of both the Ti₃O₅-Mo and the Pt/Ti₃O₅-Mo, UV-vis measurements were performed on the aqueous electrolytes of the two catalysts before and after APCT measurements, resulting in no variation in each electrolyte solution, Fig. 12, which prove that the Ti₃O₅-Mo is a very stable support in acidic electrolytes.

Finally, to assess the good performance of the Pt/Ti₃O₅-Mo catalyst, LSV and CO stripping measurements were repeated after the APCT procedure. Results in Fig. 13(a) show that the ORR activity is only slightly affected by the APCT procedure, with a shift of 0.05 V of the half-wave potential (from 0.86 to 0.81 V vs RHE). At 0.9 V vs RHE, the current density decreased from 1.1 to 0.6 mA cm⁻². From the CO stripping results, Fig. 13(b), the peak potential appearing at 0.74 V vs RHE for the fresh Pt/Ti₃O₅-Mo shifted to 0.75 V vs RHE. Their minor pre-peak at a lower potential, typical of the presence of Ti-suboxide layers [81,82], shifted as well to slightly higher potential. The calculated mass activity at 0.9 V vs RHE after APCT reached the value of 40 mA mg⁻¹. These results clearly demonstrate that the Pt/Ti₃O₅-Mo is a highly active and stable catalyst toward ORR.

4. Conclusions

A Pt/Ti₃O₅-Mo catalyst was synthesized by modifying commercial anatase TiO₂ with Mo into Ti₃O₅-Mo suboxide, and further

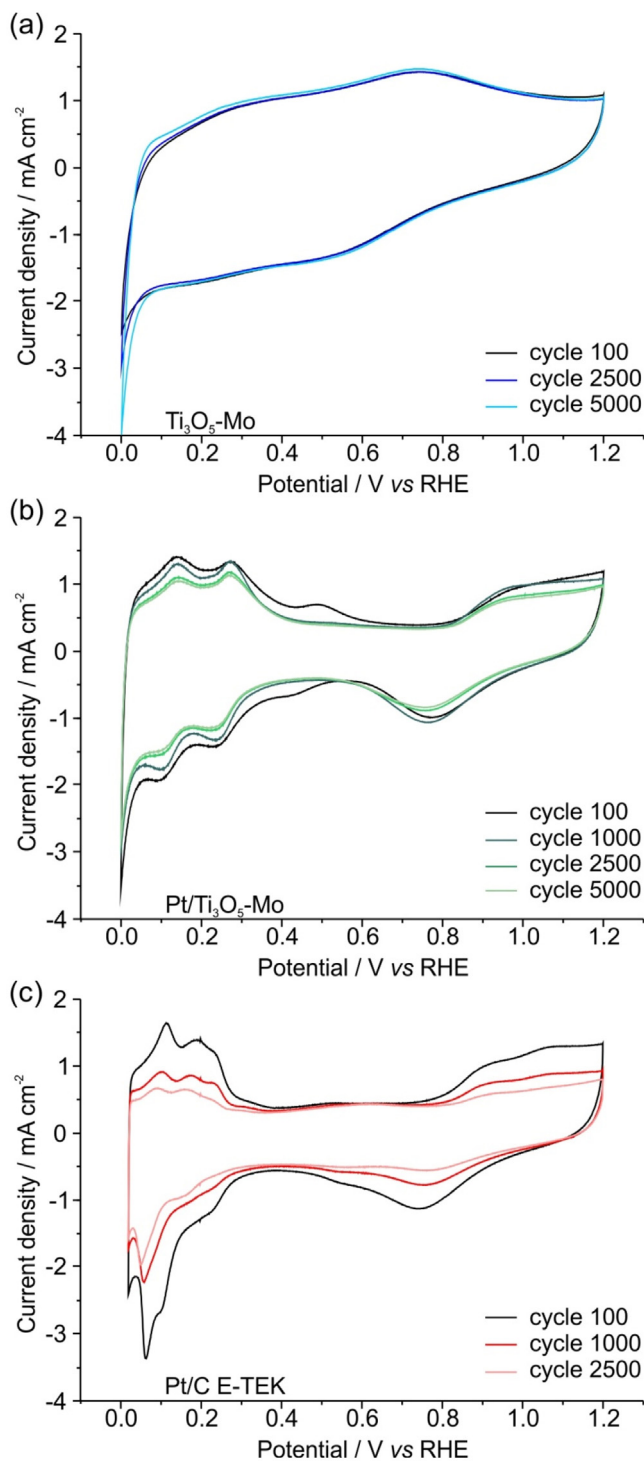


Fig. 10. APCT tests performed on (a) $\text{Ti}_3\text{O}_5\text{-Mo}$, (b) $\text{Pt}/\text{Ti}_3\text{O}_5\text{-Mo}$, and (c) Pt/C E-TEK , recorded in $0.5 \text{ M H}_2\text{SO}_4$ at 25°C , in the range $0\text{--}1.2 \text{ V vs RHE}$ at a scan rate of 50 mV s^{-1} .

deposition of 15 wt.% Pt. The Pt-based carbon-free catalyst was fully characterized and tested for the oxygen reduction reaction, using both sulfuric and perchloric acid as electrolyte. Its performance was compared to that of commercial Pt/C from E-TEK, demonstrating a good performance of 73.3 mA mg^{-1} , with a current density of 1.1 mA cm^{-2} at 0.9 V vs RHE compared to the 0.7 mA cm^{-2} at 0.9 V vs RHE of the commercial one. A deep accelerated potential cycling between 0 and 1.2 V vs RHE up to 5000 cycles demonstrated

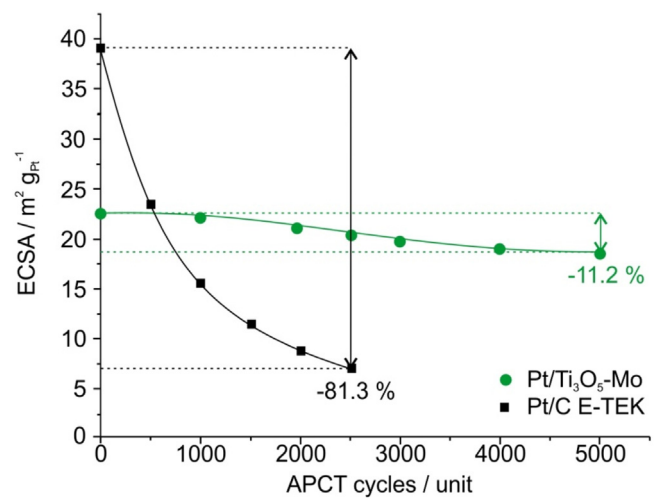


Fig. 11. ECSA trends according to APCT for the $\text{Pt}/\text{Ti}_3\text{O}_5\text{-Mo}$ and Pt/C E-TEK catalysts. Data calculated from Fig. 10(b) and (c).

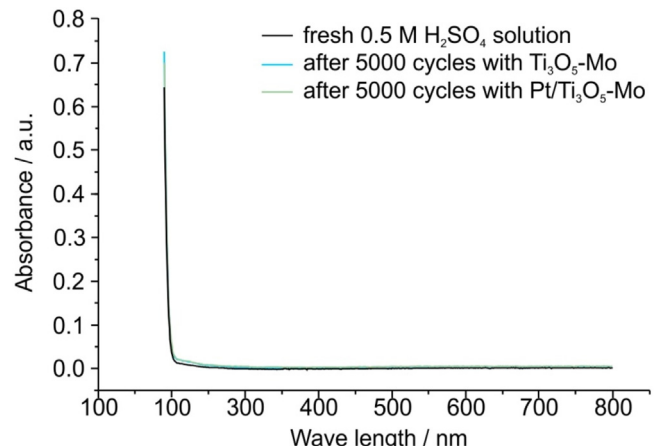


Fig. 12. UV absorption spectra of $0.5 \text{ M H}_2\text{SO}_4$ aqueous electrolyte before and after APCT tests (up to 5000 cycles) for $\text{Ti}_3\text{O}_5\text{-Mo}$ and $\text{Pt}/\text{Ti}_3\text{O}_5\text{-Mo}$.

the remarkable stability of the $\text{Pt}/\text{Ti}_3\text{O}_5\text{-Mo}$ catalyst, whose ECSA loss was accounted for only 11%, compared to the more than 81% loss of the commercial Pt/C reference, notwithstanding a starting ECSA value almost the double of the $\text{Pt}/\text{Ti}_3\text{O}_5\text{-Mo}$ catalyst. The stable performance was attributed to the positive effect of the doped $\text{Ti}_3\text{O}_5\text{-Mo}$ suboxide in stabilizing the Pt probably because of a change in the *d*-band length of the $\text{Ti}_3\text{O}_5\text{-Mo}$ support. Thus, the $\text{Pt}/\text{Ti}_3\text{O}_5\text{-Mo}$ can be considered as an innovative stable carbon-free alternative catalyst for ORR for PEMFC applications.

Acknowledgements

The results of this work belong to the Italian project PRIN NAMEDPEM (“Advanced nanocomposite membranes and innovative catalysts for durable polymer electrolyte membrane fuel cells”, protocol n. 2010CYTWAW) funded by the Italian Ministry of Education, University, and Research. The authors gratefully acknowledge Prof. P. Zelenay from the Los Alamos National Laboratory (U.S.A.) for fruitful discussions, and Prof. E. Pastor from the University of Laguna (Spain) for TEM measurements.

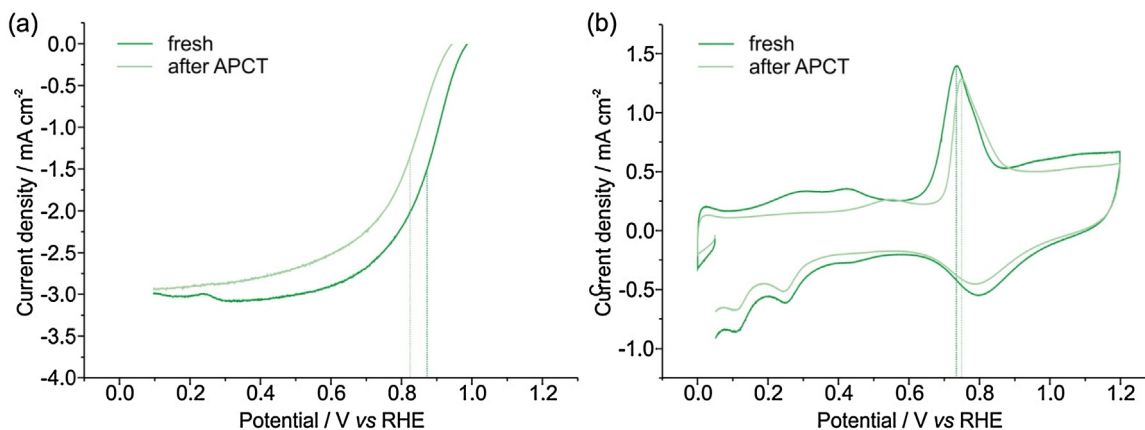


Fig. 13. (a) comparison of ORR for Pt/Ti₃O₅-Mo before and after APCT, recorded in 0.5 M H₂SO₄, scan rate of 5 mV s⁻¹ at 25 °C and 900 rpm. (b) comparison of CV of CO oxidation on Pt/Ti₃O₅-Mo before and after APCT, recorded in 0.5 M H₂SO₄, scan rate of 20 mV⁻¹ at 25 °C (for both cases, catalyst loading: 15 µgPt cm⁻², 0.1 ITC mass ratio).

References

- [1] K. Sasaki, L. Zhang, R.R. Adzic, *Phys. Chem. Chem. Phys.* 10 (2008) 159–167.
- [2] H.A. Gasteiger, S.S. Kocha, B. Sompalli, F.T. Wagner, *Appl. Catal. B: Environ.* 56 (2005) 9–35.
- [3] S. Specchia, C. Francia, P. Spinelli, in: R.S. Liu, L. Zhang, X. Sun, H. Liu, J. Zhang (Eds.), *Electrochemical Technologies for Energy Storage and Conversion*, Wiley-VCH, Weinheim, 2011, pp. 601–669.
- [4] A. Collier, H. Wang, X.Z. Yuan, J. Zhang, D.P. Wilkinson, *Int. J. Hydrogen Energy* 31 (2006) 1838–1854.
- [5] J. Parrondo, T. Han, E. Niangar, C. Wang, N. Dale, K. Adjeman, V. Ramani, *Proc. Nat. Acad. Sci.* 7 (2014) 45–50.
- [6] S.-Y. Huang, P. Ganeshan, B.N. Popov, *Appl. Catal. B: Environ.* 96 (2010) 224–231.
- [7] D. Du, J. Wu, H. Yang, *ACS Catal.* 4 (2014) 144–151.
- [8] Y. Ou, X. Cui, X. Zhang, Z. Jiang, *J. Power Sources* 195 (2010) 1365–1369.
- [9] T. Ioroi, Z. Siroma, N. Fujiwara, S.-i. Yamazaki, K. Yasuda, *Electrochim. Commun.* 7 (2005) 183–188.
- [10] F.C. Walsh, R.G.A. Wills, *Electrochim. Acta* 55 (2010) 6342–6351.
- [11] M. Tian, G. Wu, A. Chen, *ACS Catal.* 2 (2012) 425–432.
- [12] Y.-W. Lee, D.-H. Kwak, A.-R. Park, B. Roh, I. Hwang, G. Cao, K.-W. Park, *Int. J. Electrochem. Sci.* 8 (2013) 9499–9507.
- [13] I. Savych, J. Bernard d'Arbiguy, S. Subianto, S. Cavaliere, D.J. Jones, J. Rozière, *J. Power Sources* 257 (2014) 147–155.
- [14] S. Bonanni, K. Ait-Mansour, H. Brune, W. Harbich, *ACS Catal.* 1 (2011) 385–389.
- [15] A. Pătru, A. Rabis, S.E. Temmel, R. Kotz, T.J. Schmidt, *Catal. Today* 262 (2016) 161–169.
- [16] B. Abida, L. Chirchi, S. Baranton, T.W. Napporn, H. Kochkar, J.-M. Léger, A. Ghorbel, *Appl. Catal. B: Environ.* 106 (2011) 609–615.
- [17] L. Aïnouche, L. Hamadou, A. Kadri, N. Benbrahim, D. Bradai, *Solar Energy Mater. Solar Cells* 151 (2016) 179–190.
- [18] J. Jun, M. Dhayal, J.-k Shin, J.-C. Kim, N. Getoff, *Radiat. Phys. Chem.* 75 (2006) 583–589.
- [19] K. Tanaka, T. Nasu, Y. Miyamoto, N. Ozaki, S. Tanaka, T. Nagata, F. Hakoe, M. Yoshikiyo, K. Nakagawa, Y. Umetsu, K. Imoto, H. Tokoro, A. Namai, S. Ohkoshi, *Cryst. Growth Des.* 15 (2015) 653–657.
- [20] L. Xiong, M. Ouyang, L. Yan, J. Li, M. Qiu, Y. Yu, *Chem. Letters* 38 (2009) 1154–1155.
- [21] X. Li, Y. Liu, S. Ma, J. Ye, X. Zhang, G. Wang, Y. Qiu, *J. Alloys Compounds* 649 (2015) 939–948.
- [22] Y. Wu, Q. Zhang, X.g Wu, S. Qin, J. Liu, *J. Solid State Chem.* 192 (2012) 356–359.
- [23] S. Ohkoshi, Y. Tsunobuchi, T. Matsuda, K. Hashimoto, A. Namai, F. Hakoe, H. Tokoro, *Nat. Chem.* 2 (2010) 539–545.
- [24] A.A. Gusev, E.G. Avvakumov, A.Z.H. Medvedev, A.I. Masliy, *Sci. Sint.* 39 (2007) 51–57.
- [25] V.T.T. Ho, C.-J. Pan, J. Rick, W.-N. Su, B.-J. Hwang, *J. Am. Chem. Soc.* 133 (2011) 11716–11724.
- [26] S. Siracusano, V. Baglio, C. D'Urso, V. Antonucci, A.S. Aricò, *Electrochim. Acta* 54 (2009) 6292–6299.
- [27] T.-T. Nguyen, V.T.T. Ho, C.-J. Pan, J.-Y. Liu, H.-L. Chou, J. Rick, W.-N. Su, B.-J. Hwang, *Appl. Catal. B Environ.* 154–155 (2014) 183–189.
- [28] O. Lori, L. Elbaz, *Catalysts* 5 (2015) 1445–1464.
- [29] O. Kartachova, A.M. Glushenkov, Y. Chen, H. Zhang, Y. Chen, *J. Mater. Chem. A* 1 (2013) 7889–7895.
- [30] M.K. Jeon, P.J. McGinn, *J. Power Sources* 195 (2010) 2664–2668.
- [31] S. Mukerjee, S. Srinivasan S, M.P. Soriaga, J. McBreen, *J. Electrochem. Soc.* 142 (1995) 1409–1422.
- [32] R.R. Adzic, J. Zhang, K. Sasaki, M.B. Vukmirovic, M. Shao, J.X. Wang, A.U. Nilekar, M. Mavrikakis, J.A. Valerio, F. Uribe, *Top. Catal.* 46 (2007) 249–262.
- [33] L.Y. Zheng, *Sens. Actuators B* 94 (2003) 294–297.
- [34] A.C.M. Padilha, M. Osorio-Guillén, A.R. Rocha, G.M. Dalpian, TinO₂n- Magnéli phases studied using density functional theory, *Phys. Rev. B* 90 (2014) 035213.
- [35] L. Calvillo, G. Garcia, A. Paduano, O. Guillen-Villafuerte, C. Valero-Vidal, A. Vittadini, M. Bellini, A. Lavacchi, A. Agnoli, A. Martucci, J. Kunze-Liebhäuser, E. Pastor, G. Granozzi, *ACS Appl. Mater. Interf.* 8 (2015) 716–725.
- [36] R. Alipour Moghadam Esfahani, A.H.A. Monteverde Videla, S. Vankova, S. Specchia, *Int. J. Hydrogen Energy* 40 (2015) 14529–14539.
- [37] S.-Y. Huang, P. Ganeshan, B.N. Popov, *J. Am. Chem. Soc.* 2 (2012) 825–831.
- [38] H.R. Colon-Mercado, B.N. Popov, *J. Power Sources* 155 (2006) 253–263.
- [39] J. Zeng, C. Francia, C. Gerbaldi, M.A. Dumitrescu, S. Specchia, P. Spinelli, *J. Solid State Electrochem.* 16 (2012) 3087–3096.
- [40] US DOE 2014 Annual Progress Report V. Fuel Cells (accessed on Dec 2015). <http://www.hydrogen.energy.gov/annual.progress14.fuelcells.html>.
- [41] D. Olguín, E. Vallejo, A. Rubio-Ponce, *Phys. Status Solid B* 252 (2015) 659–662.
- [42] G. Rajender, P.K. Giri, *J. Alloys Compd.* 676 (2016) 591–600.
- [43] O. Yepez, B.R. Scharifker, *Int. J. Hydrogen Energy* 27 (2002) 99–105.
- [44] X. Han, F. Cheng, T. Zhang, J. Yang, Y. Hu, J. Chen, *Adv. Mater.* 26 (2014) 2047–2051.
- [45] G. Chiappe, E. Louis, E.V. Anda, J.A. Verges, *Phys. Rev. B* 71 (2005) 241405(R).
- [46] C. Zhou, J. Wu, A. Nie, R.C. Forrey, A. Tachibana, H. Cheng, *J. Phys. Chem. C* 111 (2007) 12773–12778.
- [47] Q. Cui, D.G. Musaev, K. Morokuma, *J. Chem. Phys.* 108 (1998) 8418.
- [48] P. Szarek, K. Urakami, Ch. Zhou, H. Cheng, A. Tachibana, *J. Chem. Phys.* 130 (2009) 084111.
- [49] A.H.A. Monteverde Videla, R. Alipour Moghadam Esfahani, I. Peter, S. Specchia, *Electrochim. Acta* 177 (2015) 51–56.
- [50] P. Justin, P.H.K. Charan, G. Ranga Rao, *Appl. Catal. B: Environ.* 100 (2010) 510–515.
- [51] N. Stem, L. de Souza M, D.L.A. de Faria, S.G. dos Santos Filho, *Thin Solid Films* 558 (2014) 67–74.
- [52] F. Shi, L.R. Baker, A. Hervier, G.A. Somorjai, K. Komvopoulos, *ACS Nano Lett.* 13 (2013) 4469–4474.
- [53] L.R. Baker, A. Hervier, H. Seo, G. Kennedy, K. Komvopoulos, G.A. Somorjai, *J. Phys. Chem. C* 115 (2011) 16006–16011.
- [54] X. Huang, Z. Zhao, L. Cao, Y. Chen, E. Zhu, Z. Lin, M. Li, A. Yan, A. Zettl, Y.M. Wang, X. Duan, T. Mueller, Y. Huang, *Science* 348 (2015) 1230–1234.
- [55] P. Justin, G. Ranga Rao, *Int. J. Hydrogen Energy* 36 (2011) 5875–5884.
- [56] D.M. Han, Z.P. Guo, R. Zeng, C.J. Kim, Y.Z. Meng, H.K. Liu, *Int. J. Hydrogen Energy* 34 (2009) 2426–2434.
- [57] B.A. Pereira, F. Laplante, M. Chaker, D. Guay, *Adv. Funct. Mater.* 17 (2007) 443–450.
- [58] H. Lin, C.P. Huang, W. Li, C. Ni, S. Ismat Shah, Y.-H. Tseng, *Appl. Catal. B: Environ.* 68 (2006) 1–11.
- [59] E. Shafiq, S. Esposito, M. Armandi, M. Manzoli, E. Garrone, B. Bonelli, *Microporous Mesoporous Mat.* 224 (2016) 229–238.
- [60] V.H. Mudavakkat, V.V. Atuchin, V.N. Kruchinin, A. Kayani, C.V. Ramana, *Optical Mater.* 34 (2012) 893–900.
- [61] W. Khan Alamgir, S. Ahmad, M.M. Hassan, A.H. Naqvi, *Optical Mater.* 38 (2014) 278–285.
- [62] H. Saleem, A. Habib, *J. Alloys Compd.* 679 (2016) 177–183.
- [63] G.G. Lenzi, C.V.B. Fávero, L.M.S. Colpini, H. Bernabe, M.L. Baesso, S. Specchia, O.A.A. Santos, *Desal* 270 (2011) 241–247.
- [64] M.I. Litter, *Appl. Catal. B: Environ.* 23 (1999) 89–114.
- [65] R. Liu, J.-X. Shang, F.-H. Wang, *Comput. Mater. Sci.* 81 (2014) 158–162.
- [66] S. Siracusano, A. Stassi, E. Modica, V. Baglio, A.S. Aricò, *Int. J. Hydrogen Energy* 38 (2013) 11600–11608.
- [67] G. Maniak, P. Stelmachowski, F. Zasada, W. Piskorz, A. Kotarba, Z. Sojka, *Catal. Today* 176 (2011) 369–372.
- [68] Y. Yang, X. Li, J. Chen, L. Wang, *J. Photochem. Photobiol. A* 163 (2004) 517–522.
- [69] C. Zhan, F. Chen, H. Dai, J. Yang, M. Zhong, *Chem. Eng. J.* 225 (2013) 695–703.
- [70] P.N. Ross, *J. Electrochim. Soc.* 126 (1979) 67–77.

- [71] N.M. Markovic, P.N. Ross, *J. Electroanal. Chem.* 330 (1992) 499–520.
- [72] N.M. Markovic, M. Hanson, G. McDougall, E. Yeager, *J. Electroanal. Chem. Interface Electrochem.* 214 (1986) 555–566.
- [73] K. Shinozaki, J.W. Zack, R.M. Richards, B.S. Pivovar, S.S. Kocha, *J. Electrochem. Soc.* 162 (2015) F1144–F1158.
- [74] H. Sakagami, Y. Asano, T. Ohno, N. Takahashi, H. Itoh, T. Matsuda, *Appl. Catal. A Gen.* 297 (2006) 189–197.
- [75] H. Noh, D. Wang, S. Luo, T.B. Flanagan, R. Balasubramaniam, Y. Sakamoto, *J. Phys. Chem. B* 108 (2004) 310–319.
- [76] P.A. Zosimova, A.V. Smirnov, S.N. Nesterenko, V.V. Yuschenko, W. Sinkler, J. Kocal, J. Holmgren, I.I. Ivanova, *J. Phys. Chem. C* 111 (2007) 14790–14798.
- [77] K. Senevirathne, R. Hui, S. Campbell, S. Ye, J. Zhang, *J. Electrochim. Acta* 59 (2012) 538–547.
- [78] A. Ignaszak, C. Song, W. Zhu, Y.-J. Wang, J. Zhang, A. Bauer, R. Baker, V. Neburchilov, S. Ye, S. Campbell, *Electrochim. Acta* 75 (2012) 220–228.
- [79] N.M. Markovic, B.N. Grigor, P.N. Ross, *J. Phys. Chem. B* 101 (1997) 5405–5413.
- [80] H. Kita, S. Ye, Y. Gao, *J. Electroanal. Chem.* 334 (1992) 351–357.
- [81] G.M. Haugen, M.K. Delbe, J.H. Thomas, K.A. Lewinski, G.D. Vernstrom, US patent 6,482,763,B2, Nov. 19, 2002. Suboxide fuel cell catalyst for enhanced reformate tolerance.
- [82] O. Guillén-Villafuerte, G. García, J.L. Rodríguez, E. Pastor, R. Guil-López, E. Nieto, J.L.G. Fierro, *Int. J. Hydrogen Energy* 38 (2013) 7811–7821.
- [83] B. Ruiz-Camacho, O. Martinez-Alvarez, H.H. Rodriguez-Santoyo, V. Granados-Alejo, *J. Electroanal. Chem.* 725 (2014) 19–24.
- [84] W.A. Rigdon, X. Huang, *J. Power Sources* 272 (2014) 845–859.
- [85] G. Wang, B. Huang, L. Xiao, Z. Ren, H. Chen, D. Wang, H.D. Abruna, J. Lu, L. Zhuang, *J. Am. Chem. Soc.* 136 (2014) 9643–9649.
- [86] R. Borup, J. Meyers, B. Pivovar, Y.S. Kim, R. Mukundan, N. Garland, D. Myers, M. Wilson, F. Garzon, D. Wood, P. Zelenay, K. More, K. Stroh, T. Zawodzinski, J. Boncella, J.E. McGrath, M. Inaba, K. Miyatake, M. Hori, K.-I. Ota, Z. Ogumi, S. Miyata, A. Nishikata, Z. Siroma, Y. Uchimoto, K. Yasuda, K.-i Kimijima, N. Iwashita, *Chem. Rev.* 107 (2007) 3904–3951.
- [87] S. Rudi, C. Cui, L. Gan, P. Strasser, *Electrocatal.* 5 (2014) 408–418.
- [88] J.-H. Kim, G. Kwon, H. Lim, C. Zhu, H. You, Y.-T. Kim, *J. Power Sources* 320 (2016) 188–195.
- [89] H. Liu, T. Lv, C. Zhu, Z. Zhu, *Solar Energy Mater. Solar Cells* 153 (2016) 1–8.
- [90] A. Kumar, V. Ramani, *ACS Catal.* 4 (2014) 1516–1525.
- [91] H. Duan, Q. Hao, C. Xu, *J. Power Sources* 280 (2015) 483–490.
- [92] Y. Bing, V. Neburchilov, C. Song, R. Baker, A. Guest, D. Ghosh, S. Ye, S. Campbell, J. Zhang, *Electrochim. Acta* 77 (2012) 225–231.
- [93] S.-Y. Huang, P. Ganesan, S. Park, B.N. Popov, *J. Am. Chem. Soc.* 131 (2009) 13898–13899.